AGU PUBLICATIONS

JGR

Journal of Geophysical Research: Space Physics

RESEARCH ARTICLE
10.1002/2016JA022801

Key Points:
- Occurrence probability and property of different types of auroral onset waves are determined
- Wave property does not relate to substorm strength but to plasma sheet configuration
- Wave properties are most consistent with kinetic ballooning interchange instability

Supporting Information:
- Data Set S1

Correspondence to:
Y. Nishimura,
toshi@atmos.ucla.edu

Citation:
Nishimura, Y., J. Yang, P. L. Pritchett, F. V. Coroniti, E. F. Donovan, L. R. Lyons, R. A. Wolf, V. Angelopoulos, and S. B. Mende (2016), Statistical properties of substorm auroral onset beads/rays, *J. Geophys. Res. Space Physics*, *121*, 8661–8676, doi:10.1002/2016JA022801.

Received 6 APR 2016
Accepted 30 AUG 2016
Accepted article online 2 SEP 2016
Published online 23 SEP 2016

Statistical properties of substorm auroral onset beads/rays

Y. Nishimura[1,2], J. Yang[3], P. L. Pritchett[4], F. V. Coroniti[4], E. F. Donovan[5], L. R. Lyons[1], R. A. Wolf[3], V. Angelopoulos[6], and S. B. Mende[7]

[1]Department of Atmospheric and Oceanic Sciences, University of California, Los Angeles, California, USA, [2]Department of Electrical and Computer Engineering and Center for Space Physics, Boston University, Boston, Massachusetts, USA, [3]Department of Physics and Astronomy, Rice University, Houston, Texas, USA, [4]Department of Physics and Astronomy, University of California, Los Angeles, California, USA, [5]Department of Physics and Astronomy, University of Calgary, Calgary, Alberta, Canada, [6]Department of Earth, Planets, and Space Sciences, University of California, Los Angeles, California, USA, [7]Space Science Laboratory, University of California, Berkeley, California, USA

Abstract Auroral substorms are often associated with optical ray or bead structures during initial brightening (substorm auroral onset waves). Occurrence probabilities and properties of substorm onset waves have been characterized using 112 substorm events identified in Time History of Events and Macroscale Interactions during Substorms (THEMIS) all-sky imager data and compared to Rice Convection Model–Equilibrium (RCM-E) and kinetic instability properties. All substorm onsets were found to be associated with optical waves, and thus, optical waves are a common feature of substorm onset. Eastward propagating wave events are more frequent than westward propagating wave events and tend to occur during lower-latitude substorms (stronger solar wind driving). The wave propagation directions are organized by orientation of initial brightening arcs. We also identified notable differences in wave propagation speed, wavelength (wave number), period, and duration between westward and eastward propagating waves. In contrast, the wave growth rate does not depend on the propagation direction or substorm strength but is inversely proportional to the wave duration. This suggests that the waves evolve to poleward expansion at a certain intensity threshold and that the wave properties do not directly relate to substorm strengths. However, waves are still important for mediating the transition between the substorm growth phase and poleward expansion. The relation to arc orientation can be explained by magnetotail structures in the RCM-E, indicating that substorm onset location relative to the pressure peak determines the wave propagation direction. The measured wave properties agree well with kinetic ballooning interchange instability, while cross-field current instability and electromagnetic ion cyclotron instability give much larger propagation speed and smaller wave period.

1. Introduction

Substorm auroral onset is characterized by initial brightening near the equatorward boundary of the auroral oval, often along a preexisting growth phase arc [*Akasofu*, 1964]. The growth phase arc is latitudinally narrow approximately in the east-west orientation, and the arc stays dim for a few to tens of minutes near the end of the growth phase [*Nishimura et al.*, 2011]. Then the arc shows the first auroral signature of substorm onset, which is initial brightening, and it is usually associated with ray structures along the arc [*Akasofu*, 1964]. Such ray structures are also called beads and can be characterized as an optical wave-like structure along an initial brightening arc [*Donovan et al.*, 2006; *Henderson*, 2009; *Rae et al.*, 2010] (hereinafter called substorm auroral onset waves or onset waves for convenience). Onset waves have received great attention in recent years because their properties may represent those of a near-Earth plasma sheet instability for triggering substorm onset. In fact, in situ observations in the plasma sheet have shown oscillatory magnetic fields that have been suggested to link to an instability associated with substorm onset [e.g., *Lui*, 1996; *Takahashi et al.*, 1987; *Ohtani et al.*, 1998; *Shiokawa et al.*, 2005]. Among their broadband spectra in space, the lower-frequency component of those fluctuations (several tens of seconds) seems to correspond to the frequency of the optical onset waves measured on the ground.

Although a number of studies showed existence of optical waves during substorm initial brightening, wave properties vary event by event. Perhaps the most notable difference is the wave propagation direction; it can be eastward (dawnward) [*Donovan et al.*, 2006; *Rae et al.*, 2010; *Motoba et al.*, 2012; *Gallardo-Lacourt et al.*, 2014], westward (duskward) [*Nishimura et al.*, 2014], or bidirectional (both eastward and westward)

[*Liang et al*., 2008; *Sakaguchi et al*., 2009; *Tang*, 2011]. *Kalmoni et al.* [2015] selected 17 substorms with beads and showed that beads for about half (nine) of the events propagated eastward, and the westward and bidirectional wave events are less frequent (three and two events). This suggests that the plasma sheet condition at substorm onset is not always the same or that more than one mode of instability can occur during substorm onset.

These studies raise fundamental questions on substorm auroral onset waves. So far, none of the existing studies have addressed how often onset waves occur. To evaluate the importance of onset waves on initial brightening, we should examine if all substorms are associated with waves during initial brightening or if some substorms occur without waves (hence may be triggered by a different process). Another key question is how properties of onset waves in each wave propagation direction relate to plasma sheet conditions. Wave properties and their geomagnetic activity dependence can provide a clue for understanding substorm onset instability but require a large number of events by distinguishing different propagation direction types. In the present study, we select 112 isolated substorm events and statistically determine occurrence properties of onset waves. We characterize wave properties, their geomagnetic activity dependence, and their relation to arc orientation. We also discuss possible connections to kinetic ballooning interchange instability and plasma sheet structures.

2. Method and Data Set

Substorm onset in this study is defined as an initial brightening of an auroral arc near the equatorward boundary of the auroral oval followed by poleward expansion [*Akasofu*, 1964] detected by any of the all-sky imagers of the Time History of Events and Macroscale Interactions during Substorms (THEMIS) mission [*Mende et al*., 2008] under favorable sky conditions. The imager network has 21 white-light cameras with a 3 s exposure and 256 × 256 pixels. Initial brightening marks the first moment when the auroral intensity along a growth phase arc starts to increase and evolves to auroral poleward expansion. We selected isolated substorm events, where aurora and ground magnetometer data did not show prior substorm activity for at least 30 min before onset. Events under strong solar wind driving (such as storm time substorms) are included as long as this condition is satisfied, and such events can be recognized in plots where data points are sorted by growth phase conditions (interplanetary magnetic field (IMF) B_z and B_y before onset). Pseudo-breakup events were removed by requiring that the *AL* or THEMIS *AL* index shows more than 100 nT of reduction (the same peak threshold as used by *Tanskanen* [2009]) during poleward expansion. Here poleward expansion is defined as the first auroral poleward motion that lasts more than a few minutes [*Akasofu*, 1964]. After the first poleward expansion, onset wave signatures are not present and dominant structures are a poleward expanding auroral arc, westward traveling surge, and streamers. To ensure that an initiation location of substorm onset is fully contained within available imager fields of view (FOVs), initial brightening should occur within an ~200 km horizontal extent from imager zenith at 110 km altitude (above ~25° elevation angle). This condition allows for having a few kilometer horizontal resolution, which is sufficiently high for resolving a typical onset wavelength of ~100 km [e.g., *Donovan et al*., 2006] and for evaluating wave existence and propagation properties. Under those selection criteria, we surveyed THEMIS all-sky imager data from 2006 to 2015 and identified 112 events. Those events are listed in the Data Set S1 in the supporting information. Differences from the event selection by *Kalmoni et al.* [2015] are that a much larger number of events are used and that pseudo-breakup events are excluded.

Onset waves were identified as two or more of luminosity structures aligned quasiperiodically along an initial brightening arc between the first appearance of the luminosity structures (i.e., onset waves) and initiation of poleward expansion (this time interval Δt is called wave duration). During this time period, the initial brightening arc essentially stays at the onset latitude without poleward expansion and waves propagate along the initial brightening arc. If all those quasiperiodic luminosity structures propagated eastward or westward within available imager FOVs, those were classified as eastward or westward propagating wave events. If both eastward and westward waves were present, those events were classified as bidirectional. Events with irregular luminosity structures, if any, were considered as "no wave" events. Wave propagation velocities along initial brightening arcs, wavelengths, and wave periods (at 110 km altitude) were recorded by tracing the onset waves in keograms along the onset arc. A set of keogram slices along the onset arc but at slightly different latitudes were used so that waves can be captured even if wave

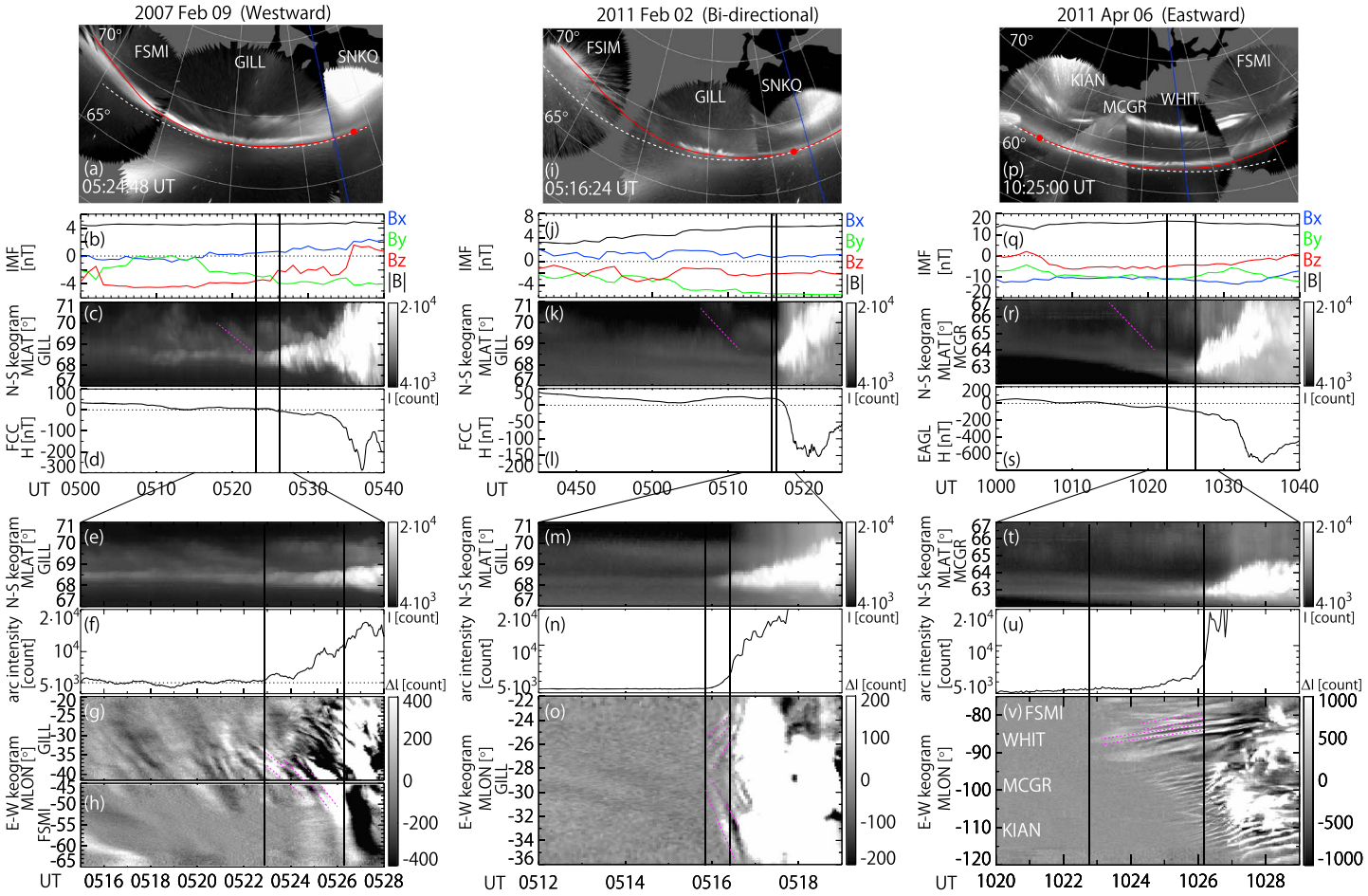

Figure 1. Three types of onset wave propagation. (a–h) Westward, (i–o) bidirectional, and (p–v) eastward propagation events. Figures 1a, 1i, and 1p shows the imager snapshot mosaics during onset wave formation. The red lines trace the initial brightening arcs and then shifted slightly equatorward for not hiding the arcs. The white dashed lines are the latitude isocontours, and the red dots mark the tangential points between the two lines. The blue lines show the magnetic midnight. The OMNI IMF (Figures 1b, 1j, and 1q), north-south keograms (Figures 1c, 1k, and 1r), and *H* component (1d, 1l, and 1s) of magnetometer data at longer time scales are shown. The vertical line marks the auroral substorm onset time. The north-south keograms (Figures 1e, 1m, and 1t), maximum intensity along the onset arc (Figures 1f, 1n, and 1u), and east-west keograms in 5 min detrended intensity scales around onset times (Figures 1g, 1h, 1o, and 1v) are shown. The first and second vertical lines mark the initial brightening and initiation of poleward expansion. The pink lines in Figures 1c, 1k, and 1r trace the preonset auroral forms propagating equatorward. The pink lines in Figures 1g and 1h, 1o, and 1v trace the representative onset waves. North-south keograms use maximum intensity within ±15° longitude from imager zenith longitude at each latitude. East-west keograms are sliced along the initial brightening arcs.

latitudinal locations change over time. When more than one keogram detect onset waves, we use the one for each wave propagation direction that shows most intense waves (generally near the low-altitude edge of an arc). The azimuthal mode number was calculated as the circumference of a circle around the Earth at onset latitude divided by the wavelength. Since waves just after their initiation are sometimes too faint to trace, we used the second half of wave durations for obtaining wave velocities, wavelengths, and periods. While these quantities usually stay the same during each event, averaged values over time were used to represent each event even when these quantities change in time. Since onset wave intensity typically grows exponentially [*Voronkov et al.*, 2003; *Rae et al.*, 2010], wave growth rate γ was obtained by calculating $\log_e(I_2/I_1)/(t_2 - t_1)$, where I_1 and I_2 are the maximum intensity counts along an initial brightening arc in the middle of an onset wave duration ($t = t_1$) and at initiation of poleward expansion ($t = t_2$), respectively. Note that onset waves are distinguished from preonset waves, which are much fainter (a few tens of counts) without intensifying in time. The arc continues to move equatorward (i.e., no poleward expansion) during those waves. Onset waves are much more intense (>~100 counts) and their amplitude increases in time. Onset waves evolve to poleward expansion.

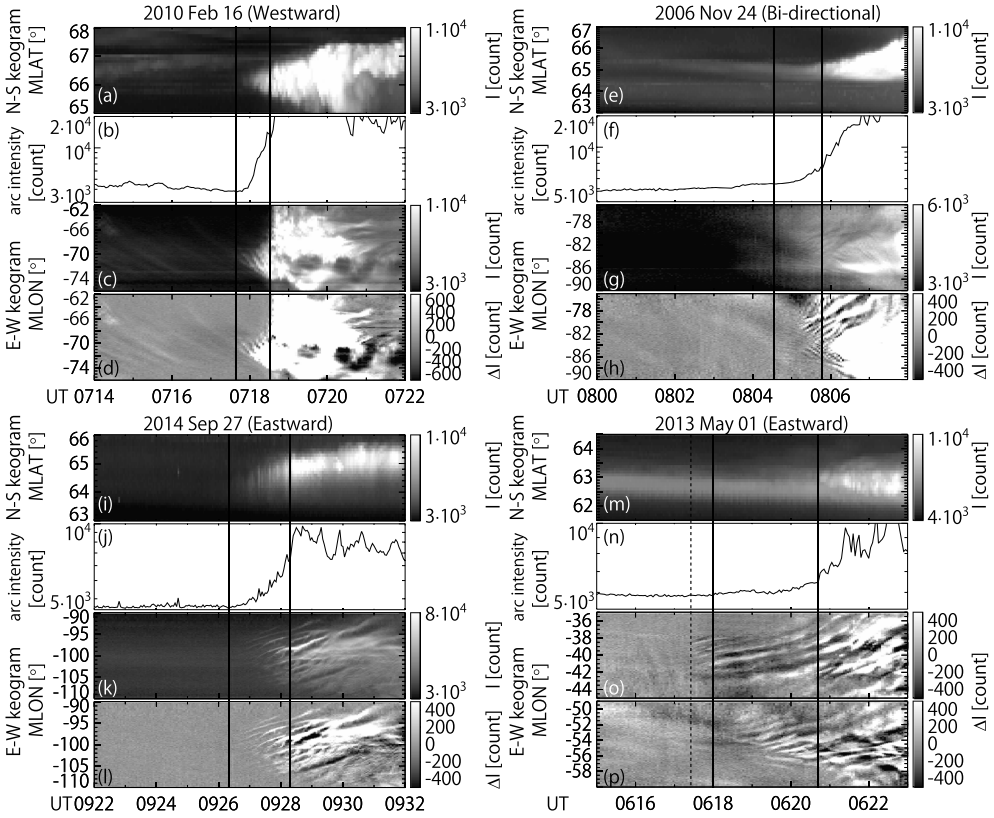

Figure 2. Four additional events of onset waves. (a–d) Westward, (e–h) bidirectional, and (i–p) eastward propagation events. From top to bottom, plots shown are north-south keograms, maximum intensity along the onset arc, and east-west keograms in (Figures 2c, 2g, and 2k) absolute and (Figures 2d, 2h, 2i, 2o, and 2p) 5 min detrended intensity scales.

3. Case Study

Figure 1 shows the three representative events of onset waves with different propagation directions (Figures 1a–1h: westward, Figures 1i–1o: bidirectional, and Figures 1p–1v: eastward propagation). The imager snapshots in Figures 1a, 1i, and 1p were taken during onset wave formation. Figures 1b, 1j, and 1q; 1c, 1k, and 1r; and 1d, 1l, and 1s show the overviews of substorm conditions. The substorm onset can be identified as sudden brightening emerging from quiet background, followed by poleward expansion. Times of initial brightening and initiation of poleward expansion are marked by the vertical lines. The *H* component of magnetometer data started to decrease substantially around the onset times and showed negative bays. The interplanetary magnetic field (IMF) B_z was southward for >15 min before the onset times. Though outside the scope of this study, equatorward propagating auroral structures can be seen just poleward of each growth phase arc in Figures 1c, 1k, and 1r (traced by pink lines), and those are preonset auroral streamers similar to the ones shown by *Nishimura et al.* [2010].

The rest of the plots show the north-south keograms, maximum intensities along the growth phase arcs, and east-west keograms around onset times. The first vertical line in each event marks the initial rise of auroral intensity (Figures 1f, 1n, and 1u), i.e., initial brightening, and it coincides with intensification of optical waves (Figures 1g, 1h, 1o, and 1v). The westward propagating wave case had preexisting waves propagating from high to low magnetic longitudes (MLONs) along the growth phase arc without changing wave intensity and then started to intensify without changing the wavelength (Figure 1g). The entire east-west extent of the waves (except a small gap between the two imagers) was covered by the available imagers. The bidirectional wave case did not have notable waves prior to the onset, but waves emerged at the initial brightening (Figure 1o). Waves on the eastern side (>~−29° MLON) propagated eastward, and waves on the western side (<~−29° MLON) propagated westward. In the eastward propagating wave event (Figure 1v), the waves emerged initially in an ~5° longitude range and then propagated eastward, while the wave occurrence region

Table 1. Number of Events, Occurrence Probability, and Properties of Waves in Each Wave Propagation Direction Category[a]

	Westward	Bidirectional	Eastward	No Wave
Number of events	26	38	48	0
Probability (%)	23.2	33.9	42.9	0
IMF B_z (nT)	-3.6 ± 0.7	-3.4 ± 1.1	-4.7 ± 1.5	-
MLAT (deg)	67.1 ± 0.5	67.0 ± 1.1	65.6 ± 1.4	-
MLT (h)	22.1 ± 0.9	22.7 ± 0.4	22.7 ± 0.6	-
ΔAL (nT)	-258 ± 188	-193 ± 73	-251 ± 108	-
Speed (km/s)	4.6 ± 1.5	-	2.8 ± 1.4	-
Wavelength (km)	98.7 ± 28.7	-	65.1 ± 15.6	-
Wave number (m^{-1})	$(6.4 \pm 1.9) \times 10^{-5}$	-	$(9.6 \pm 2.3) \times 10^{-5}$	-
Mode number	155 ± 44	-	252 ± 55	-
Period (s)	18 ± 6	-	23 ± 10	-
Duration (s)	69 ± 33	81 ± 34	84 ± 35	-
Growth rate (s^{-1})	0.04 ± 0.03	0.04 ± 0.02	0.03 ± 0.02	-

[a]The wave properties are characterized by median and quartiles.

also spread westward. The wave propagation was slower than in the westward propagation event. The waves continued to grow at least until the initiation of the poleward expansion (second vertical lines). The wave signatures can still be found during the early phase of poleward expansion, but the wave intensity, wavelength, and propagation speed change and become irregular. While the wave occurrence region spread azimuthally, the wavelength and propagation speed stayed almost the same until the initiation of the poleward expansion. The latitudinal extent of the initial brightening arc was essentially the same as the growth phase arc until initiation of the poleward expansion.

In the imager snapshots (Figures 1a, 1i, and 1p), we visually traced the low-altitude edge of the onset arcs as by the red lines (and slightly shifted down for visualization). Considering the observation geometry from the ground, the arc low-altitude edge is projected as the low-latitude edge when viewing equatorward, while the arc high-latitude edge corresponds to the low-altitude edge when viewing poleward. Minimum latitude points of the onset arcs are marked by the red dots. The onset arcs are mostly east-west oriented but are slightly tilted. The onset waves in the westward propagating wave event occurred to the west of the minimum latitude point. The waves in the bidirectional event also occurred to the west but with a smaller tilt of the onset arc. In contrast, the eastward propagating wave event occurred to the east of the minimum latitude point. Another difference we noticed is the onset latitude. The onsets in the westward and bidirectional wave events occurred at typical substorm onset latitudes (~67° magnetic latitude (MLAT) [*Liou et al.*, 2001; *Frey et al.*, 2004]), while the onset of the eastward propagating wave event occurred at lower latitudes (63°–64° MLAT). We statistically investigate in section 4 whether such differences are seen in general.

Four more events of onset waves are shown in Figure 2. Event sequences of the westward propagating (Figures 2a–2d), bidirectional (Figures 2e–2h), and eastward propagating (Figures 2i–2p) events are essentially the same as in the Figure 1 events, indicating that the wave properties mentioned above represent typical features of onset waves. However, while the optical wave initiation generally coincides with initial brightening, waves occasionally form earlier than initial brightening. An example is shown in Figures 2m–2p. While optical waves appeared at the time of the dashed vertical line, the auroral brightness did not change until initial brightening (the first solid vertical line), meaning that this is not a brightening or a brightening that is too small compared to the background arc luminosity so that this is rather recognized as structuring of the previously homogeneous growth phase arc. After the initial brightening (first solid vertical line), the sequence was the same as in the Figures 2i–2l event; the waves became more intense without changing the wavelength or phase and spread azimuthally until the initiation of the poleward expansion (second solid vertical line). The existence of waves before the initial brightening is similar to the westward propagating wave cases (Figures 1a–1h and 2a–2d), although the wave duration prior to the initial brightening in the Figures 2m–2p case was much shorter. The smooth continuation of those preexisting waves to the onset waves indicates that those are precursor waves to substorm initial brightening in a similar manner to the westward wave cases [*Nishimura et al.*, 2014].

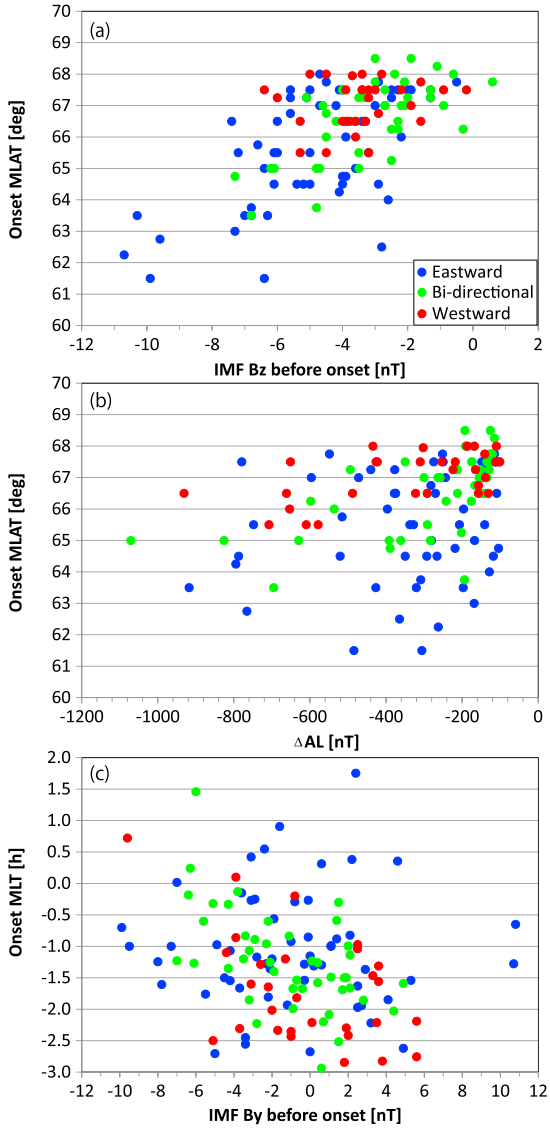

Figure 3. Scatterplots between (a) onset MLAT and IMF B_z before onset, (b) onset MLAT and ΔAL, and (c) onset MLT and IMF B_y (median B_y within 30 min before onset). The red, green, and blue dots indicate the westward, bidirectional, and eastward propagating waves.

4. Statistical Study

4.1. Geomagnetic Conditions

We have examined wave existence and wave propagation direction of each substorm event listed in Data Set S1. Table 1 summarizes the occurrence of wave propagation directions and wave properties. Nearly half the events (42.9%) show eastward propagation. The second biggest category is bidirectional, and the rest of the events are westward propagating. The occurrence probabilities are roughly consistent with the study by *Kalmoni et al.* [2015]. Within our data set, all events showed onset waves, indicating that optical waves are common features of substorm onset.

Figure 3 shows the dependence of wave propagation directions on geomagnetic conditions and onset locations. In Figure 3a, propagation directions are shown as functions of IMF B_z before onset (minimum B_z within 60 min before onset and 60 min being a typical growth phase duration [*Li et al.*, 2013]) and onset MLAT. The onset latitude shifts equatorward with stronger solar wind driving [*Liou et al.*, 2001]. Most events occurring below 65° MLAT are eastward propagating events, and each wave propagation direction at typical onset latitudes (~67° MLAT) occurs almost equally. Similarly, most events under large southward IMF show eastward propagation. This tendency indicates that plasma sheet conditions related to the solar wind energy input during the growth phase are important for determining wave propagation directions.

Figure 3b plots the data points as functions of ΔAL and onset MLAT. ΔAL is used as a measure of substorm strengths and was calculated as a minimum of AL-AL_{onset} within 30 min after onset, where AL_{onset} is the AL at auroral onset time. THEMIS AL was used instead when it was negatively larger than the standard AL. The 30 min threshold was set to be longer than a typical substorm expansion phase duration (~16 min [*Chu et al.*, 2015]). Westward and bidirectional wave events show a weak correlation between the onset latitude and substorm strength, meaning that those wave events follow the relation between the growth phase energy input and substorm strength presented in earlier studies [*Li et al.*, 2013; *Sergeev et al.*, 2015]. In contrast, data points of eastward waves are scattered without any trend, and thus, eastward propagating wave events do not appear to relate to substorm strength.

Figure 3c shows the IMF B_y-magnetic local time (MLT) dependence of the wave propagation directions. The westward and bidirectional wave events tend to occur at earlier MLTs with increasing IMF B_y, which is consistent with the result by *Liou et al.* [2001]. The eastward propagating wave events, however, do not have a clear dependence on the IMF B_y, although those events on average occur at slightly later MLT (by ~0.6 h MLT; see Table 1).

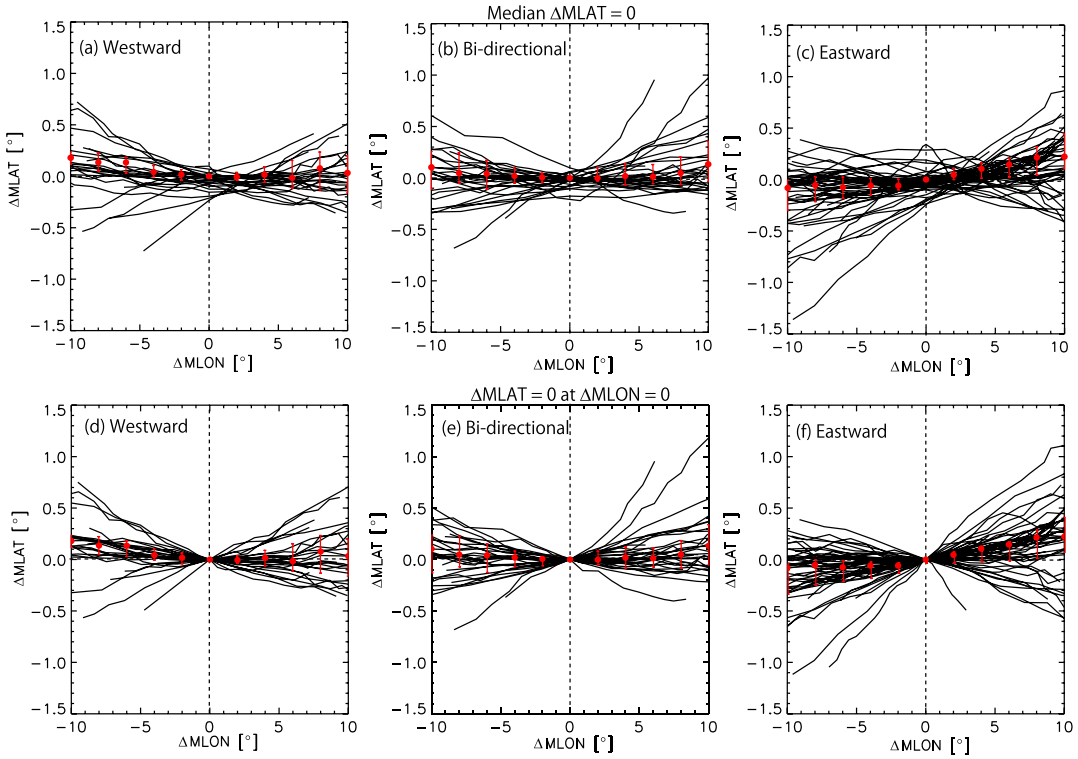

Figure 4. Superposed plots of onset arc orientation in the AACGM magnetic coordinates. The longitude is given relative to each imager zenith longitude. (a–c) Plots subtract median MLAT of each line, while (d–f) plots set ΔMLAT = 0 at ΔMLON = 0. (Figures 4a and 4d) Westward, (Figures 4b and 4e) bidirectional, and (Figures 4c and 4f) eastward propagating wave events. The red dots and vertical bars show the median and quartiles every 2° MLON.

4.2. Arc Orientation

We recorded initial brightening arc orientation near substorm onset time as in Figure 1 and created superposed plots for each wave propagation direction as shown in Figure 4. Each imager zenith longitude was used as a reference longitude, and a median latitude of each event was subtracted in Figures 4a–4c. The same data are used in Figures 4d–4f except that ΔMLAT was set to 0 at ΔMLON = 0. Since the quartiles (red bars) are close to the medians (red dots) except near the edges of each plot, the medians can reasonably represent the arc orientation. The arcs in the westward propagation, bidirectional, and eastward propagation events are oriented from northwest to southeast, essentially azimuthally, and from northeast to southwest, respectively. This tendency can also be seen in the cases shown in Figure 1.

Considering that quiet auroral arcs are not strictly east-west oriented but have minimum latitudes near midnight [*Gillies et al.*, 2014], the Figure 4 results suggest that onset wave propagation directions are related to onset location relative to the minimum latitude point: onset events close to the minimum latitude point tend to show bidirectional propagations, while onset events to the west and east of the minimum latitudes tend to show waves propagating westward and eastward, respectively. This means that wave propagation directions are related to magnetotail configuration during the substorm growth phase. We discuss this issue in section 5.2.

4.3. Wave Properties

As mentioned in section 2, wave properties (east-west propagation velocity, wavelength, azimuthal mode number, period, duration, and growth rate) were obtained by tracing wave-like luminosity structures along the initial brightening arcs. Median properties are listed in Table 1. Some of bidirectional wave properties are not characterized because the degree of mixture between westward and eastward waves affects calculations.

Figure 5 shows the wave properties as functions of onset MLAT and ΔAL. The east-west propagation velocity, wavelength, period, and duration show notable differences between westward and eastward propagating wave events. Westward propagating wave events tend to have larger azimuthal propagation speeds, longer

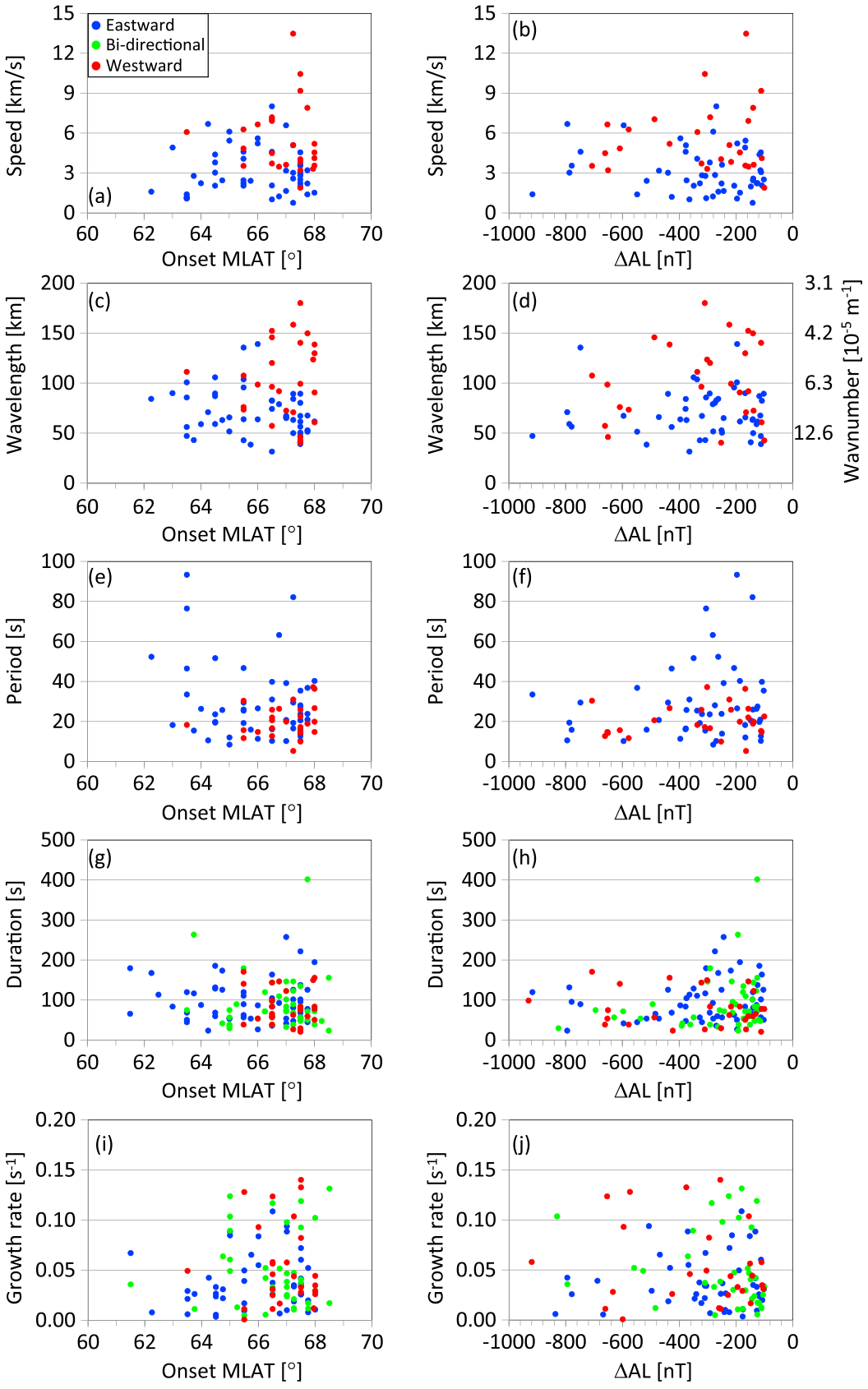

Figure 5. Onset wave properties as functions of (a, c, e, g, and i) onset MLAT and (b, d, f, h, and j) ΔAL.

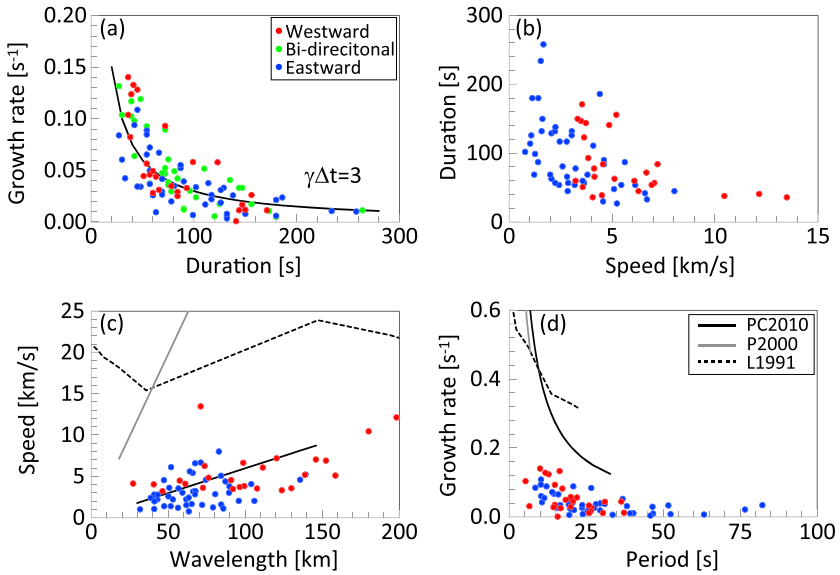

Figure 6. (a–d) Selected plots of correlations among onset wave parameters. The black line in Figure 6a is a fit by $\gamma = 8/\Delta t$ curve. The black solid, grey, and dashed lines in Figures 6c and 6d indicate the kinetic model predictions by PC2010, P2010, and L1991, respectively.

azimuthal wavelengths, shorter period, and shorter duration compared to eastward propagating wave events. The growth rate is about the same for all propagation directions (~0.03–0.04 s^{-1}). The median numbers obtained here are roughly consistent with those in the past studies [*Donovan et al.*, 2006; *Tang*, 2011; *Chang and Cheng*, 2015; *Kalmoni et al.*, 2015].

Since there is no data point in the top left corners of Figures 5b, 5d, 5f, and 5h, large substorms tend to have smaller wave velocities, shorter wavelengths, shorter periods, and shorter durations than small substorms. For the same reason in Figures 5a, 5c, and 5h, substorms under larger solar wind driving tend to have smaller velocities, shorter wavelengths, and smaller growth rates. In contrast, the growth rate does not have clear dependence on ΔAL or wave propagation direction. This indicates that wave growths are not strongly related to the substorm expansion phase.

Figure 6 shows the scatterplots of selected combinations of wave properties. The highest correlation was found between the wave growth rate and wave duration (Figure 6a). The growth rate is negatively correlated with the wave duration, meaning that waves with larger growth rates evolve more quickly to poleward expansion while waves with smaller growth rates last longer. The data points approximately follow the $\gamma\Delta t = 3$ curve, and thus, waves evolve to poleward expansion at a common level of exponential growth after initial brightening regardless of the growth rate. Similarly, the duration of the wave growth is longer for slower propagating waves (Figure 6b). This is consistent with the result of Figures 5i and 5j, where the wave growth rate does not relate to solar wind energy input or substorm intensity but waves evolve into the poleward expansion stage at a certain threshold independent of the growth rate or duration. The wavelength is roughly proportional to the wave velocity (Figure 6c), and the growth rate is larger for shorter periods (Figure 6d). These relations are compared to kinetic instability properties in section 5.1.

4.4. Wave Formation Timing

As shown in Figures 1 and 2, substorm onset waves initiate at initial brightening for most events. However, as shown in Figures 2m–2p, optical waves can initiate slightly earlier than the initial brightening. There are six such events (5.4% of 112 events; wave initiation times are indicated as T_0 in Data Set S1), and the median time difference between the wave initiation and initial brightening is 101 s. All those events are eastward propagating waves. Since only a small fraction of events shows such wave formation before initial brightening, we cannot determine the importance of such waves. However, in analogy to westward propagating waves before initial brightening that last much longer [*Nishimura et al.*, 2014], the eastward propagating

waves before initial brightening may also indicate preonset waves that are stable but can potentially become unstable through additional processes such as flows from further downtail.

5. Discussion

5.1. Comparison to Kinetic Instability Properties

Here we compare wave properties found in Figure 6 with instability in the near-Earth plasma sheet to evaluate possible instability from an auroral point of view. Because the wavelength, when mapped to the plasma sheet, is of the order of an ion gyroradius (see below), kinetic effects should be considered for evaluating possible instability processes. Among possible kinetic instability processes, we consider cross-field current instability, electromagnetic ion cyclotron instability, and kinetic ballooning interchange instability because these waves have been shown to agree well with waves measured in the near-Earth plasma sheet [*Lui*, 1996; *Le Contel et al*., 2000; *Panov et al*., 2012] and wave properties have been documented in detail [*Lui et al*., 1991; *Perraut et al*., 2000; *Pritchett and Coroniti*, 2010]. While similar evaluations have been made on case and multievent study bases [*Rae et al*., 2010; *Kalmoni et al*., 2015], we use a larger number of events and consider kinetic ballooning interchange instability.

Pritchett and Coroniti [2010] (hereinafter PC2010) showed that a dominant unstable mode of kinetic ballooning interchange instability in the near-Earth plasma sheet can be characterized as $k_y\rho_i = 6.3$, $\omega_r/k_y v_{Ti} = 0.125$, $\omega_r/\Omega_{i0} = 0.21$, and $\gamma/\Omega_{i0} = 0.13$. Here k_y is the cross-tail wave number, ρ_i is the ion gyroradius, Ω_{i0} is the ion gyrofrequency in a reference (lobe) magnetic field (B_0), ω_r is the real part of the wave frequency, γ is the growth rate, and v_{Ti} is the ion thermal speed. This mode propagates duskward with a wavelength comparable to the ion gyroradius. The ballooning mode has been extensively studied in both kinetic and fluid regimes, and similar properties have been presented in other literatures [*Miura et al*., 1989; *Zhu et al*., 2003; *Cheng*, 2004; *Klimushkin et al*., 2012]. While electromagnetic ion cyclotron instability can occur in a wide frequency range, it was mainly considered for waves near the proton gyrofrequency [*Le Contel et al*., 2000]. Such waves were indeed shown to grow in a kinetic simulation by *Pritchett et al.* [2014], who parameterized those waves as $k_y\rho_i = 2.6$, $\omega_r/k_y v_{Ti} = 0.5$, and $\omega_r/\Omega_i = 0.96$, where Ω_i is the local ion gyrofrequency. The corresponding growth rate in *Perraut et al.* [2000] (hereinafter P2000) is $\gamma/\Omega_i \sim 0.5$. Properties of cross-field current instability are not as conveniently parameterized, but Figure 8 of *Lui et al.* [1991] (hereinafter L1991) showed parameter dependence as $k\rho_e \sim 0.035 - 0.27$, $\theta \sim 30° - 90°$, $\omega_r/\omega_{LH} \sim 0.015 - 0.33$, and $\gamma/\omega_{LH} \sim 0.0073 - 0.017$ within an ω_{pe}/Ω_e range of 5 and 55, where θ is the wave normal angle, ρ_e is the local electron gyroradius, ω_{LH} is the lower hybrid frequency, ω_{pe} is the electron plasma frequency, and Ω_e is the electron gyrofrequency.

We compare the properties they found and our statistical results in Figures 6c and 6d. For P2000 and PC2010, the ion temperature dependence of the equations above gives wavelength-velocity relations shown as black lines in Figure 6c, where ion temperature is changed between 8 and 20 keV and the lobe magnetic field strength is 20 nT. Lobe magnetic field dependence gives relations between the wave growth rate and period as in the lines in Figure 6d, where the field strength is changed between 20 and 60 nT (the plasma sheet magnetic field is roughly 1/3–1/4 of the lobe magnetic field). The magnetic field strength and plasma sheet temperature are known to change as functions of solar wind conditions [*Forsyth et al*., 2014; *Tsyganenko*, 2000], and thus, these parameters would roughly simulate different growth phase conditions. In L1991, the plasma density and ion temperature are fixed to 0.6 cm^{-3} and 12 keV. Under this density value, the ω_{pe}/Ω_e range corresponds to a 4.5–50 nT magnetic field range in the plasma sheet, which gives a fair comparison to the magnetic field range for PC2010 and P2000. Temperature dependence of L1991 parameterizations is not given. For all these three waves, the propagation speed and wavelengths in the plasma sheet were mapped to the ionosphere using the T01 magnetic field model [*Tsyganenko*, 2002] using the solar wind conditions of the Figure 1 cases, and averaged mapping factors of those three events were used. The onset location is assumed to be at ~8 R_E near midnight [*Sergeev et al*., 2012]. Ions are assumed as protons.

Since the kinetic waves studied in those modeling studies propagate duskward, here we only compare to measured westward propagating waves (see below for a discussion of eastward propagating waves). The best agreement with the observations was found in kinetic ballooning by PC2010. The PC2010 results explain

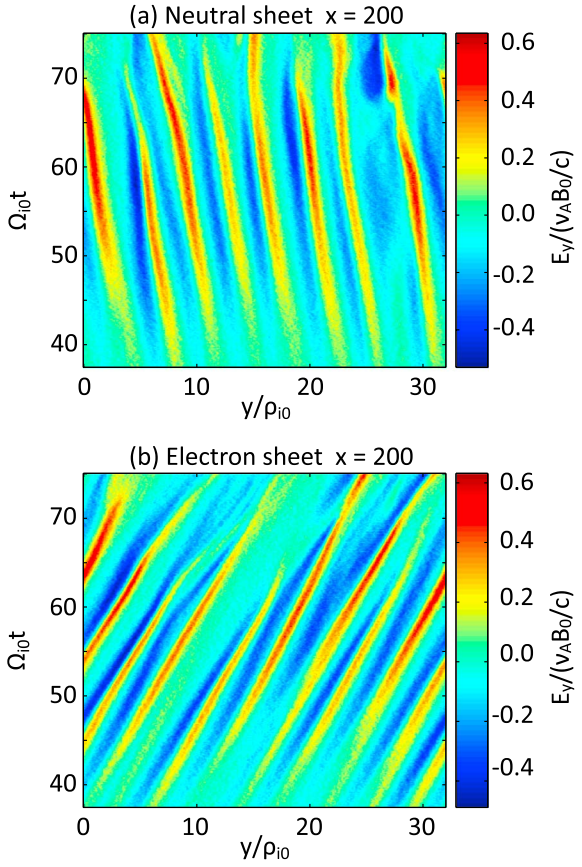

Figure 7. Kinetic simulation results of kinetic ballooning wave growth in dawn-dusk electric field (normalized E_y) along the cross-tail direction on the equatorial plane. (a) Same setup as in PC2010 with a charge-neutral current sheet and (b) an electron current sheet were used.

the wavelength-velocity relation very well (Figure 6c). The growth rate by PC2010 is a factor of ~2–3 larger but gives the closest estimate among the three model curves. The predicted wave period is in good agreement with the observations. In contrast, the L1991 results give much larger wave propagation speed and growth rate, and the wave period is somewhat underestimated, although the wavelength is comparable to the observations. The quantitative agreements between PC2010 and our observations suggest that the kinetic ballooning interchange instability can be considered as a potential mechanism to explain measured properties of substorm onset waves.

Note, however, that the PC2010 results have dependence on the lobe density and current sheet thickness [*Pritchett and Coroniti*, 2013], and mapping to the ionosphere largely depends on onset location and magnetic field configuration. Thus, the lines in Figures 6c and 6d are not fixed but vary depending on plasma sheet conditions. Such factors may contribute to the scatter of the data points, and we cannot expect perfect agreement between the observations and model predictions. We did not compare to shear flow-related instabilities such as shear flow ballooning instability [*Voronkov et al*., 2003] because the width and strength of shear flows are not well known. As discussed in section 5.2, flow directions may play a role in determining wave propagation directions, and thus, flow-related instabilities may also be important for driving onset waves.

The treatment of the kinetic ballooning instability in PC2010 envisioned only waves propagating in the direction of the ion drift (westward), and thus, it provides no explanation of the eastward propagating waves. This limitation was also pointed out by *Kornilov et al.* [2016], who reported both eastward and westward propagating waves. We now demonstrate, however, that a modification of the treatment in PC2010 can provide a kinetic ballooning explanation of the eastward propagating waves as well. Figure 7 shows the structures and propagation of the electric field of kinetic ballooning waves in the crosstail direction (Y) as a function of time on the equatorial plane using the particlein-cell simulation developed by PC2010. The selected X location of 200 corresponds to the tailward gradient region of B_z, where kinetic ballooning waves first appear. Figure 7a uses the same setup as PC2010, where the current sheet is initially in equilibrium and charge neutral. The ion and electron drifts are in opposite directions, with the relative magnitudes determined by the ion to electron temperature ratio. Westward propagating wave growth is found as expected. Another simulation run was performed (Figure 7b), where the cross-tail current is carried only by the eastward drifting electrons; the ions have no drift. In order for this configuration to be in equilibrium, one must include an E_z electric field in order to confine the nonuniform ion density distribution. This polarization field is produced by a (slight) excess of electrons over ions, so that the current sheet is charged. The current sheet thickness in this new run is the same as that in the original PC2010 simulation. It was shown by *Pritchett and Coroniti* [1995] that such electron-dominated current sheets are

naturally formed within the larger-scale plasma sheet during periods of convection driven by an externally imposed E_y field, and such embedded current sheets have been observed in the magnetotail [e.g., *Petrukovich et al*., 2011]. From Figure 7b it is clear that waves with a similar wavelength and growth rate are produced, but now they propagate eastward. The eastward drift of waves arises from eastward $E \times B$ drifts by equatorward E_z. The wave propagation speed, however, is larger by a factor of about 2–3 than that for the westward waves in Figure 7a. Since such embedded thin current sheets are expected to dominate under stronger solar wind driving, the Figure 7b results may explain the dominance of eastward propagating waves under larger IMF B_z. However, the wavelength and propagation speed results are not consistent with the results in Figure 6c. Since these properties will depend on the details of the plasma sheet configuration, it is clear that further investigation of the properties of eastward propagating kinetic ballooning waves under different conditions is needed.

5.2. Comparison to Rice Convection Model

To interpret the relation between arc orientation and magnetotail structures, we refer to Rice Convection Model–Equilibrium (RCM-E) results. Figures 8a–8e show the configuration at the end of a 65 min idealized substorm growth phase. The simulation setup is essentially the same as in *Yang et al.* [2013]. We start from a T89 empirical magnetic field model with $Kp = 1$ [*Tsyganenko*, 1989] and an empirical plasma pressure model [*Lemon et al*., 2003] that has been relaxed to a state of equilibrium. The boundary conditions are time independent. A 65 kV cross-polar cap potential drop is applied to the RCM simulation region; thus, a steady earthward convection is modeled in the growth phase. The plasma distribution function along the RCM high-latitude boundary has a local minimum at midnight. The magnetic field and the plasma pressure are kept in force balance through the simulation.

The secondary pressure peak at 7–8 R_E radial distance, which corresponds to growth phase field-aligned currents (FACs; Figures 8a and 8d), is almost symmetric in the dawn-dusk direction with a maximum slightly shifted to postmidnight. When mapping to the ionosphere, the FAC sheets have minimum latitudes near midnight, where the sheets in the premidnight sector are oriented from northwest to southeast and the sheets in the postmidnight sector are oriented from northeast to southwest. Those orientations are consistent with the measured arc orientations shown in Figure 1, and a comparison with Figure 4 shows that the westward, bidirectional, and eastward propagating waves occur in the premidnight upward FAC region, near the transition region, and in the postmidnight upward FAC region, respectively. Thus, the arc orientation and wave propagation direction can be associated with the pressure peak in the near-Earth plasma sheet and substorm onset location relative to the pressure peak.

Figures 8f–8j show another RCM-E run with twice as hot population at the tailward boundary. While the overall structures are the same, the secondary pressure peak at 7–8 R_E radial distance shifts toward premidnight due to larger ion magnetic drifts. The transition between the premidnight- and postmidnight-type FACs also shifts duskward by ~1 R_E in the plasma sheet or by ~0.3 h MLT in the ionosphere (Figures 8e and 8j). The duskward shift of the pressure and FAC patterns indicate that the postmidnight-type upward FAC region extends toward the premidnight sector, where substorms occur more often than in the postmidnight sector and increases the probability of eastward propagating wave events. Since the plasma sheet temperature increases with solar wind energy input [*Forsyth et al*., 2014], larger temperature in the plasma sheet could be the reason of the higher occurrence of eastward propagating waves under stronger solar wind driving (Figure 3a).

The wave propagation directions are qualitatively consistent with the flow directions shown in Figure 8c. The flow vectors are a combination of $E \times B$ and diamagnetic drifts using equation (3) of *Yang et al.* [2012]. Since the $E \times B$ drift in this case is essentially sunward (see equipotential contours of Figure 8a), the azimuthal flows in the FAC regions are mostly diamagnetic drifts. The vectors are directed duskward in the premidnight upward FAC region (X~-8–-10 R_E and $Y > 0$), and dawnward in the postmidnight upward FAC region (X~-7 R_E and $Y < 0$), even though ion ∇B and curvature drifts in both duskside and dawnside FAC regions are directed westward (not shown). Although we do not have knowledge of instability processes in dawnward diamagnetic drift regions, diamagnetic drifts may contribute to drive instability of eastward propagating waves. This inference is consistent with theoretical investigations, showing that ballooning waves propagate in ion diamagnetic drift directions [*Miura et al*., 1989; *Zhu et al*., 2003; *Cheng*, 2004; *Klimushkin et al*., 2012].

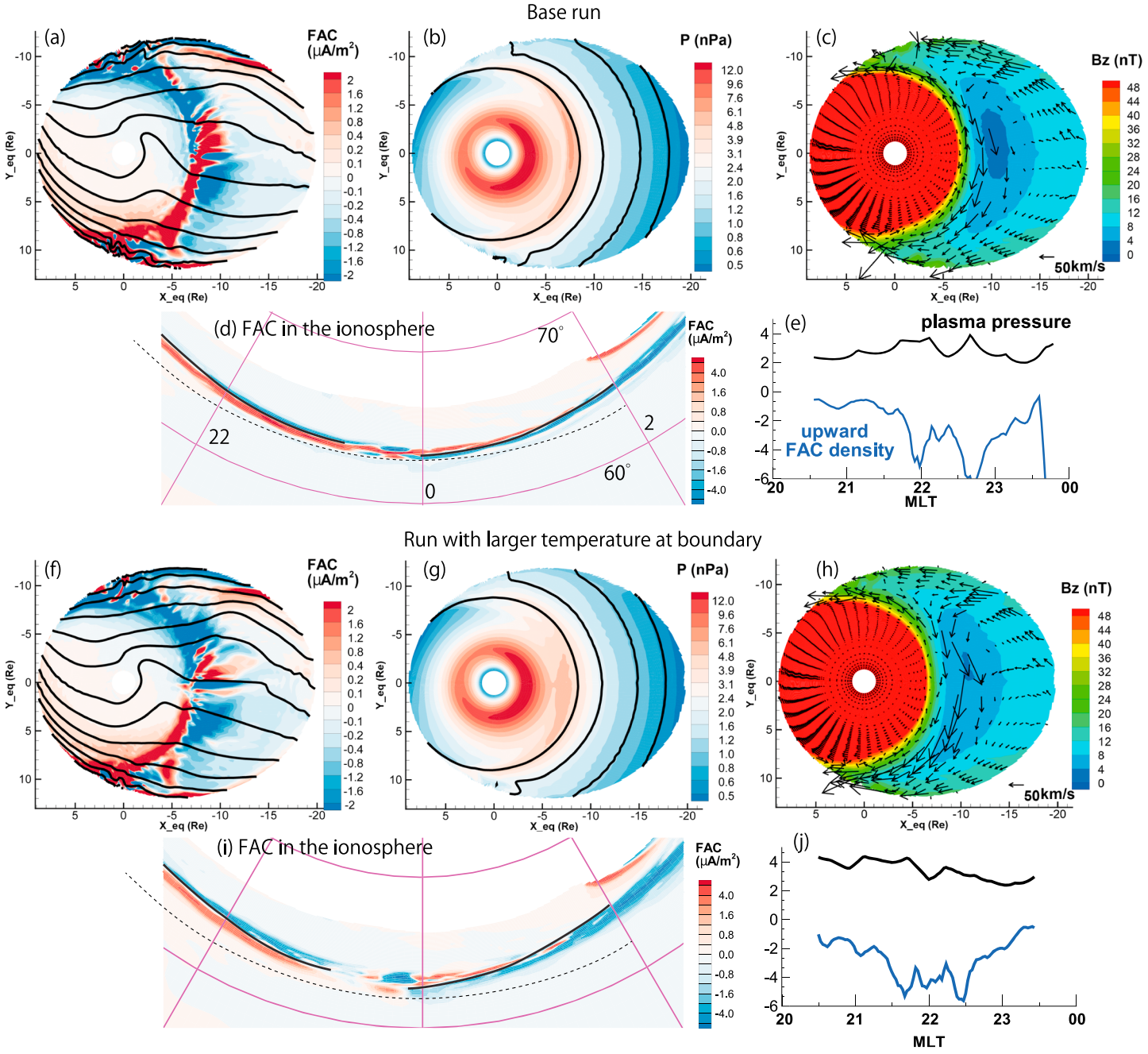

Figure 8. RCM-E run results (top) of the base run and (bottom) with twice as hot population at the tailward boundary after reaching equilibrium. (a and f) FACs mapped to the equatorial plane and equipotential contours without corotation every 5 kV, (b and g) equatorial thermal pressure and flux tube volume contours every 0.2 R_E/nT, (c and h) equatorial B_z and flow ($E \times B$ and diamagnetic combined) vectors, (d and i) FACs in the ionosphere, and (e and j) plasma pressure and upward FAC along the center of the upward FAC. The solid lines in Figures 8d and 8i trace the large-scale boundaries between upward (blue) and downward (red) FACs, and the dashed lines are the latitude isocontours.

6. Conclusion

We examined occurrence probabilities and properties of substorm auroral onset waves during substorm initial brightening using 112 substorm events identified in THEMIS all-sky imager data. The statistical results are summarized in Table 1. We found that all substorms in our data set are associated with optical waves along initial brightening arcs, indicating that those waves commonly occur during substorm onset. Eastward propagating waves are most dominant, but bidirectional and westward propagating waves also

occupy certain fractions of events. Eastward propagating events are more dominant under large southward IMF during the growth phase and hence for substorms that occur at lower latitudes. The wave propagation direction is strongly related to the orientation of initial brightening arcs. The arcs are roughly east-west oriented, but each arc has a minimum latitude near midnight, and westward, bidirectional, and eastward propagating waves occur to the west, near, and to the east of the minimum latitude point.

The wave occurrence characteristics and their relation to arc orientation indicate that propagation directions of onset waves are affected by magnetotail configuration. By comparing to the RCM-E modeling the arc orientation can be interpreted as structures of near-Earth plasma pressure and FACs: substorm onset location relative to the pressure peak determines the wave propagation direction. The wave propagation directions are parallel to the diamagnetic drift directions, and thus, diamagnetic drifts may play a role in exciting the waves. The pressure peak and FAC locations shift duskward in a hotter plasma sheet, which is expected under stronger solar wind driving. This would increase a chance of interaction between magnetotail flows and eastward propagating waves (dawnside upward FAC region) and may explain the dominance of eastward propagating wave events in lower-latitude substorm events.

Eastward and westward propagating waves have notable differences in wave properties as summarized in Table 1. However, the median growth rate is essentially the same for all propagation direction categories. The wave growth rate also does not depend on substorm strength. Instead, the growth rate is inversely proportional to the wave duration. This means that the wave growth evolves to poleward expansion at a common level of exponential growth. These properties suggest that wave growths do not determine substorm strengths but only signify the transition between the substorm growth phase and auroral poleward expansion, although the waves can still be considered as a key feature of substorm onset. The growth rate is smaller for lower-latitude onset events.

The measured wave properties were compared to cross-field current instability, electromagnetic ion cyclotron instability, and kinetic ballooning interchange instability. The kinetic ballooning interchange instability by PC2010 gives the best prediction of the measured properties of westward waves, while the other instabilities give much larger propagation speed and smaller wave period. This agreement indicates that kinetic ballooning may play a crucial role for triggering the substorm auroral onset waves, and kinetic effects are important because the wavelength is comparable to the ion gyroradius. Note, however, that this comparison concerns westward propagating waves and that a separate consideration is necessary for understanding eastward propagating waves. The flow and FAC patterns in the RCM-E modeling showed that the diamagnetic drift directions are consistent with the wave propagation directions. Properties of eastward waves are substantially different from westward waves, and thus, a different type of plasma sheet processes may be related to eastward waves. We presented possibilities that an embedded current sheet and eastward diamagnetic drifts in the dawnside upward FACs may be related to eastward propagating waves. If background flows are present, those may also contribute to change wave propagation direction.

Acknowledgments

This work was supported by NASA grants NNX12AJ57G, NNX13AI61G, NNX14AN55G, NNX15AI62G, NNX14AF70G, and NAS5-02099; NSF grants AGS-1004736, PLR-1341359, AGS-1451911, AGS-1401822, and AFOSR FA9550-15-1-0179; and CSA contract 9F007-046101. THEMIS imager data were obtained from http://themis.ssl.berkeley.edu as daily CDF files. OMNI and geomagnetic indices data were downloaded as CDF files through http://cdaweb.gsfc.nasa.gov. RCM-E outputs can be requested from J.Y. and R.A.W., and kinetic simulation outputs can be obtained from P.L.P. and F.V.C.

References

Akasofu, S.-I. (1964), The development of the auroral substorm, *Planet. Space Sci.*, *12*, 273–282, doi:10.1016/0032-0633(64)90151-5.

Chang, T. F., and C. Z. Cheng (2015), Relationship between wave-like auroral arcs and Pi2 disturbances in plasma sheet prior to substorm onset, *Earth Planets Space*, *67*, 168, doi:10.1186/s40623-015-0334-8.

Cheng, C. Z. (2004), Physics of substorm growth phase, onset, and dipolarization, *Space Sci. Rev.*, *113*, 207–270, doi:10.1023/B:SPAC.0000042943.59976.0e.

Chu, X., R. L. McPherron, T.-S. Hsu, and V. Angelopoulos (2015), Solar cycle dependence of substorm occurrence and duration: Implications for onset, *J. Geophys. Res. Space Physics*, *120*, 2808–2818, doi:10.1002/2015JA021104.

Donovan, E., S. B. Mende, B. Jackel, M. Syrjäsuo, M. Meurant, I. Voronkov, H. U. Frey, V. Angelopoulos, and M. Connors (2006), The azimuthal evolution of the substorm expansive phase onset aurora, in *Proceedings of the Eighth International Conference on Substorms*, edited by M. Syrjäsuo and E. Donovan, pp. 55–60, Univ. of Calgary, Calgary, Alberta, Canada.

Forsyth, C., et al. (2014), Increases in plasma sheet temperature with solar wind driving during substorm growth phases, *Geophys. Res. Lett.*, *41*, 8713–8721, doi:10.1002/2014GL062400.

Frey, H. U., S. B. Mende, V. Angelopoulos, and E. F. Donovan (2004), Substorm onset observations by IMAGE-FUV, *J. Geophys. Res.*, *109*, A10304, doi:10.1029/2004JA010607.

Gallardo-Lacourt, B., Y. Nishimura, L. R. Lyons, J. M. Ruohoniemi, E. Donovan, V. Angelopoulos, K. A. McWilliams, and N. Nishitani (2014), Ionospheric flow structures associated with auroral beading at substorm auroral onset, *J. Geophys. Res. Space Physics*, *119*, 9150–9159, doi:10.1002/2014JA020298.

Gillies, D. M., D. J. Knudsen, E. F. Donovan, E. L. Spanswick, C. Hansen, D. Keating, and S. Erion (2014), A survey of quiet auroral arc orientation and the effects of the interplanetary magnetic field, *J. Geophys. Res. Space Physics*, *119*, 2550–2562, doi:10.1002/2013JA019469.

Henderson, M. G. (2009), Observational evidence for an inside-out substorm onset scenario, *Ann. Geophys.*, *27*, 2129–2140, doi:10.5194/angeo-27-2129-2009.

Kalmoni, N. M. E., I. J. Rae, C. E. J. Watt, K. R. Murphy, C. Forsyth, and C. J. Owen (2015), Statistical characterization of the growth and spatial scales of the substorm onset arc, *J. Geophys. Res. Space Physics*, *120*, 8503–8516, doi:10.1002/2015JA021470.

Klimushkin, D. Y., P. N. Mager, and V. A. Pilipenko (2012), On the ballooning instability of the coupled Alfvén and drift compressional modes, *Earth Planets Space*, *64*, 777–781, doi:10.5047/eps.2012.04.002.

Kornilov, I. A., T. A. Kornilova, and I. V. Golovchanskaya (2016), Peculiarities of the azimuthal propagation of perturbations in discrete auroral arcs during the substorm growth phase, *Geomagn. Aeron.*, *56*(2), 187–194, doi:10.1134/S0016793216010096.

Le Contel, O., S. Perraut, A. Roux, R. Pellat, and A. Korth (2000), Substorms in the inner plasma sheet, *Adv. Space Res.*, *25*(12), 2395–2406, doi:10.1016/S0273-1177(99)00529-3.

Lemon, C., F. R. Toffoletto, M. Hesse, and J. Birn (2003), Computing magnetospheric force equilibria, *J. Geophys. Res.*, *108*(A6), 1237, doi:10.1029/2002JA009702.

Li, H., C. Wang, and Z. Peng (2013), Solar wind impacts on growth phase duration and substorm intensity: A statistical approach, *J. Geophys. Res. Space Physics*, *118*, 4270–4278, doi:10.1002/jgra.50399.

Liang, J., E. F. Donovan, W. W. Liu, B. Jackel, M. Syrjäsuo, S. B. Mende, H. U. Frey, V. Angelopoulos, and M. Connors (2008), Intensification of preexisting auroral arc at substorm expansion phase onset: Wave-like disruption during the first tens of seconds, *Geophys. Res. Lett.*, *35*, L17S19, doi:10.1029/2008GL033666.

Liou, K., P. T. Newell, D. G. Sibeck, C.-I. Meng, M. Brittnacher, and G. Parks (2001), Observation of IMF and seasonal effects in the location of auroral substorm onset, *J. Geophys. Res.*, *106*, 5799–5810, doi:10.1029/2000JA003001.

Lui, A. T. Y. (1996), Current disruption in the Earth's magnetosphere: Observations and models, *J. Geophys. Res.*, *101*, 13,067–13,088, doi:10.1029/96JA00079.

Lui, A. T. Y., C.-L. Chang, A. Mankofsky, H.-K. Wong, and D. Winske (1991), A cross-field current instability for substorm expansions, *J. Geophys. Res.*, *96*, 11,389–11,401, doi:10.1029/91JA00892.

Mende, S. B., S. E. Harris, H. U. Frey, V. Angelopoulos, C. T. Russell, E. Donovan, B. Jackel, M. Greffen, and L. M. Peticolas (2008), The THEMIS array of ground-based observatories for the study of auroral substorms, *Space Sci. Rev.*, *141*, 357–387, doi:10.1007/s11214-008-9380-x.

Miura, A., S. Ohtani, and T. Tamao (1989), Ballooning instability and structure of diamagnetic hydromagnetic waves in a model magnetosphere, *J. Geophys. Res.*, *94*, 15,231–15,242, doi:10.1029/JA094iA11p15231.

Motoba, T., K. Hosokawa, A. Kadokura, and N. Sato (2012), Magnetic conjugacy of northern and southern auroral beads, *Geophys. Res. Lett.*, *39*, L08108, doi:10.1029/2012GL051599.

Nishimura, Y., L. Lyons, S. Zou, V. Angelopoulos, and S. Mende (2010), Substorm triggering by new plasma intrusion: THEMIS all-sky imager observations, *J. Geophys. Res.*, *115*, A07222, doi:10.1029/2009JA015166.

Nishimura, Y., L. R. Lyons, V. Angelopoulos, T. Kikuchi, S. Zou, and S. B. Mende (2011), Relations between multiple auroral streamers, pre-onset thin arc formation, and substorm auroral onset, *J. Geophys. Res.*, *116*, A09214, doi:10.1029/2011JA016768.

Nishimura, Y., et al. (2014), Coordinated ionospheric observations indicating coupling between pre-onset flow bursts and waves that leads to substorm onset, *J. Geophys. Res. Space Physics*, *119*, 3333–3344, doi:10.1002/2014JA019773.

Ohtani, S., K. Takahashi, T. Higuchi, A. Lui, H. Spence, and J. Fennell (1998), AMPTE/CCE-SCATHA simultaneous observations of substorm-associated magnetic fluctuations, *J. Geophys. Res.*, *103*, 4671–4682, doi:10.1029/97JA03239.

Panov, E. V., V. A. Sergeev, P. L. Pritchett, F. V. Coroniti, R. Nakamura, W. Baumjohann, V. Angelopoulos, H. U. Auster, and J. P. McFadden (2012), Observations of kinetic ballooning/interchange instability signatures in the magnetotail, *Geophys. Res. Lett.*, *39*, L08110, doi:10.1029/2012GL051668.

Perraut, S., O. Le Contel, A. Roux, and A. Pedersen (2000), Current-driven electromagnetic ion cyclotron instability at substorm onset, *J. Geophys. Res.*, *105*, 21,097–21,107, doi:10.1029/2000JA900059.

Petrukovich, A. A., A. V. Artemyev, H. V. Malova, V. Y. Popov, R. Nakamura, and L. M. Zelenyi (2011), Embedded current sheets in the Earth's magnetotail, *J. Geophys. Res.*, *116*, A00I25, doi:10.1029/2010JA015749.

Pritchett, P. L., and F. V. Coroniti (1995), Formation of thin current sheets during plasma sheet convection, *J. Geophys. Res.*, *100*, 23,551–23,565 , doi:10.1029/95JA02540.

Pritchett, P. L., and F. V. Coroniti (2010), A kinetic ballooning/interchange instability in the magnetotail, *J. Geophys. Res.*, *115*, A06301, doi:10.1029/2009JA014752.

Pritchett, P. L., and F. V. Coroniti (2013), Structure and consequences of the kinetic ballooning/interchange instability in the magnetotail, *J. Geophys. Res. Space Physics*, *118*, 146–159, doi:10.1029/2012JA018143.

Pritchett, P. L., F. V. Coroniti, and Y. Nishimura (2014), The kinetic ballooning/interchange instability as a source of dipolarization fronts and auroral streamers, *J. Geophys. Res. Space Physics*, *119*, 4723–4739, doi:10.1002/2014JA019890.

Rae, I. J., C. E. J. Watt, I. R. Mann, K. R. Murphy, J. C. Samson, K. Kabin, and V. Angelopoulos (2010), Optical characterization of the growth and spatial structure of a substorm onset arc, *J. Geophys. Res.*, *115*, A10222, doi:10.1029/2010JA015376.

Sakaguchi, K., K. Shiokawa, and E. Donovan (2009), Azimuthal structures of ray auroras at the beginning of auroral substorms, *Geophys. Res. Lett.*, *36*, L23106, doi:10.1029/2009GL041252.

Sergeev, V., Y. Nishimura, M. Kubyshkina, V. Angelopoulos, R. Nakamura, and H. Singer (2012), Magnetospheric location of the equatorward prebreakup arc, *J. Geophys. Res.*, *117*, A01212, doi:10.1029/2011JA017154.

Sergeev, V. A., N. P. Dmitrieva, N. A. Stepanov, D. A. Sormakov, V. Angelopoulos, and A. V. Runov (2015), On the plasma sheet dependence on solar wind and substorms and its role in magnetosphere-ionosphere coupling, *Earth Planets Space*, *67*, 133, doi:10.1186/s40623-015-0296-x.

Shiokawa, K., I. Shinohara, T. Mukai, H. Hayakawa, and C. Z. Cheng (2005), Magnetic field fluctuations during substorm-associated dipolarizations in the nightside plasma sheet around $X = -10\ R_E$, *J. Geophys. Res.*, *110*, A05212, doi:10.1029/2004JA010378.

Takahashi, K., L. J. Zanetti, R. E. Lopez, R. W. McEntire, T. A. Potemra, and K. Yumoto (1987), Disruption of the magnetotail current sheet observed by AMPTE/CCE, *Geophys. Res. Lett.*, *14*, 1019–1022, doi:10.1029/GL014i010p01019.

Tang, C. L. (2011), The wave-like auroral structure around auroral expansion onset, *Chin. Phys. Lett.*, *28*(10), 109411, doi:10.1088/0256-307X/28/10/109401

Tanskanen, E. I. (2009), A comprehensive high-throughput analysis of substorms observed by IMAGE magnetometer network: Years 1993–2003 examined, *J. Geophys. Res.*, *114*, A05204, doi:10.1029/2008JA013682.

Tsyganenko, N. A. (1989), Magnetospheric magnetic field model with a warped tail current sheet, *Planet. Space Sci.*, *37*, 5–20, doi:10.1016/0032-0633(89)90066-4.

Tsyganenko, N. A. (2000), Solar wind control of the tail lobe magnetic field as deduced from Geotail, AMPTE/IRM, and ISEE 2 data, *J. Geophys. Res.*, *105*, 5517–5528, doi:10.1029/1999JA000375.

Tsyganenko, N. A. (2002), A model of the magnetosphere with a dawn-dusk asymmetry: 1. Mathematical structure, *J. Geophys. Res.*, *107*(A8), 1179, doi:10.1029/2001JA000219.

Voronkov, I. O., E. F. Donovan, and J. C. Samson (2003), Observations of the phases of the substorm, *J. Geophys. Res.*, *108*(A2), 1073, doi:10.1029/2002JA009314.

Yang, J., F. R. Toffoletto, R. A. Wolf, S. Sazykin, P. A. Ontiveros, and J. M. Weygand (2012), Large-scale current systems and ground magnetic disturbance during deep substorm injections, *J. Geophys. Res.*, *117*, A04223, doi:10.1029/2011JA017415.

Yang, J., R. A. Wolf, F. R. Toffoletto, and S. Sazykin (2013), RCM-E simulation of substorm growth phase arc associated with large-scale adiabatic convection, *Geophys. Res. Lett.*, *40*, 6017–6022, doi:10.1002/2013GL058253.

Zhu, P., A. Bhattacharjee, and Z. . W. Ma (2003), Hall magnetohydrodynamic ballooning instability in the magnetotail, *Phys. Plasmas*, *10*, 249–258, doi:10.1063/1.1526830.